Valence photoionization of noble-gas atoms confined in the fullerene C_{60}

Mohammad H. Javani,[1] Himadri S. Chakraborty,[2] and Steven T. Manson[1,*]

[1]*Department of Physics & Astronomy, Georgia State University, Atlanta, Georgia 30303, USA*

[2]*Center for Innovation and Entrepreneurship, Department of Natural Sciences, Northwest Missouri State University, Maryville, Missouri 64468, USA*

(Received 21 November 2013; published 5 May 2014)

A systematic study and comparison of the photoionization cross sections of the outer and inner shells of the noble-gas atoms He, Ne, Ar, Kr, and Xe confined endohedrally inside a C_{60} molecule are calculated by employing a time-dependent local-density-approximation formulation. Confinement resonances are found to be a general feature of these cross sections and dramatic interchannel coupling effects, significantly increasing the atomic cross sections, are exhibited in all cases in the vicinity of the C_{60} plasmons. Hybridization effects, the mixing of the atomic and cage bound-state wave functions, are also found, but no systematics of the hybridization present themselves.

DOI: 10.1103/PhysRevA.89.053402 PACS number(s): 36.40.Cg, 33.80.Eh, 61.48.−c

I. INTRODUCTION

The study of the photoionization of systems composed of atoms entrapped in fullerene molecules, termed endohedral fullerenes [1], is an increasingly active field of inquiry [2–4]. From a technological point of view, there is the promise of applications in a wide range of areas, including quantum computing [5], drug delivery [6], photovotaic materials [7], and hydrogen storage [8], to cite a few. In addition, these studies allow us to understand how a trapped atom responds to an external stimulus; in this case the trap is the fullerene cage. Most of the investigations that have been performed have been theoretical [2–4], but recently experimental studies have been reported [9–12].

Theoretical studies have been carried out using several different models for the interaction of the enclosed atom with the surrounding fullerenes [2–4] and these models have been incorporated in a variety of theoretical techniques [2–4,13–21]. A number of different confined systems have been looked at in these various theoretical studies. In this paper we report on a systematic study of the photoionization of the outer and near outer shells of the noble-gas atoms He, Ne, Ar, Kr, and Xe confined in the C_{60} fullerene. The aim is to elucidate the similarities and differences of the effects of confinement across the set of noble-gas atoms.

Since the interest is in low-energy photoionization, starting at the threshold of the valence shells, it is crucial to employ a theoretical model that includes coupling of the atomic photoionization channels with the huge low-energy plasmon resonances of the surrounding fullerene [22]. Furthermore, since the valence electron wave functions of an atom are typically of large spatial extent, it is necessary to allow for the possibility of mixing of the initial-state wave functions of the atom with those of the C_{60} shell, i.e., hybridization of the atomic wave functions. In addition, the inclusion of correlation is of importance to ensure the accuracy of the calculations. A methodology that includes all of these effects is our jellium-based time-dependent local-density technique, which includes interchannel coupling, hybridization, and significant aspects of correlation [18]. This methodology has been used in the past and has predicted a huge cross-section increase in atomic photoionization channels owing to the interaction with the plasmons of C_{60} (interchannel coupling) [23–25] along with significant effects of hybridization [18,26,27].

Thus, as mentioned above, both hybridization of atomic electron wave functions with shell electron wave functions and interchannel coupling between atomic and shell plasmon channels have been found previously; in this paper the focus is upon how these effects propagate along the series of the various noble-gas atoms entrapped in C_{60}. In addition, confinement resonances have been known for two decades [28]: Their explanation was presented more than ten years ago [29] and these were recently analyzed in photoelectron momentum space to reveal details of the molecular geometry [30]; again here, their manifestation in the photoionization cross section over a broad range of inner and outer shell is studied. In other words, the motivation is to provide some perspective as to how these effects behave along a series of related endohedrals, to discover other aspects of endohedral atoms and their photoionization, and to provide theoretical data for an array of targets and subshells as a stimulus for experiment.

In the following section, a brief discussion of the theory and calculational methodology are presented. In Sec. III a detailed account of the results is presented and discussed. Section IV includes a summary, conclusions, and some prospects for further work.

II. CALCULATION

Nonrelativistic density-functional theory is used to obtain the structure of the C_{60} fullerene cage. In the formulation for the C_{60} ground state, the four valence electrons ($2s^2 2p^2$) of each carbon atom are delocalized (a total of 240 delocalized electrons), while the core C^{4+} ions (each consisting of a carbon nucleus plus two very tightly bound $1s$ electrons) are represented by a classical spherical jellium shell (with radius $R = 3.54$ Å and thickness Δ) and a constant potential depth V_0 [28]; details of the calculation were presented in Ref. [18]. The energy levels and designations (in harmonic-oscillator notation) of the electronic states of the free C_{60} molecule are

*smanson@gsu.edu

TABLE I. Calculated binding energies of the occupied states of free C_{60} in atomicunits.

State	Binding energy
$1s$	−1.392378
$1p$	−1.369104
$1d$	−1.322853
$1f$	−1.254177
$1g$	−1.163832
$1h$	−1.052725
$1i$	−0.921855
$1j$	−0.772279
$2s$	−0.645068
$2p$	−0.618723
$1k$	−0.605075
$2d$	−0.567211
$2f$	−0.491933
$1l$	−0.421323
$2g$	−0.394359
$2h$	−0.276164

shown in Table I. The entrapped noble-gas atom is placed at the center of the C_{60} shell and the Kohn-Sham equations for the $(240 + N)$-electron system (240 cage electrons and $N = 2$ for He, $N = 10$ for Ne, $N = 18$ for Ar, $N = 36$ for Kr, and $N = 54$ for Xe) are then solved to obtain the ground-state wave function of the system in the local-density approximation (LDA). A widely used parametric exchange-correlation potential is used in the calculation [31]. The parameters V_0 and Δ are determined by requiring both charge neutrality and obtaining the experimental value of 7.54 eV for the first ionization potential. This procedure yields $\Delta = 1.5$ Å, in excellent agreement with experiment [32].

To remove the unphysical self-interactions in the LDA potential, a self-interaction correction was introduced into the potential [33]. The importance of doing this is that the potential with this correction has the correct asymptotic form. However, since the self-interaction correction is orbital dependent, this renders the LDA potential orbital specific, i.e., electrons in the different states are subject to somewhat different potentials.

A time-dependent LDA (TDLDA) method [18,22] is employed to calculate the dynamical response of the system to the external dipole field, i.e., the photoionization cross section. The perturbation z, the dipole interaction for linearly polarized light, induces a frequency-dependent complex change in the electron density arising from dynamical electron correlations. This can be written, using the LDA susceptibility χ_0, as

$$\delta\rho(\vec{r};\omega) = \int \chi_0(\vec{r},\vec{r}';\omega)\delta V(\vec{r}';\omega)d\vec{r}' \tag{1}$$

with

$$\begin{aligned}\delta V(\vec{r}';\omega) &= z + \delta V'(\vec{r}';\omega) \\ &= z + \int \frac{\delta\rho(\vec{r}';\omega)}{|\vec{r} - \vec{r}'|}d\vec{r}' + \left[\frac{\partial V_{xc}}{\partial\rho}\right]_{\rho=\rho_0}\delta\rho(\vec{r};\omega),\end{aligned} \tag{2}$$

where the second and third terms on the right-hand side are, respectively, the induced change of the Coulomb and the exchange-correlation potentials. In addition to the external perturbation z, δV also includes the dynamical field produced by important electron correlations. The photoionization cross section is then calculated as the sum of independent partial cross sections $\sigma_{nl\to kl'}$ corresponding to a dipole transition $nl \to kl'$ as

$$\sigma_{PI} = \sum_{nl}\sigma_{nl\to kl'} \approx \sum_{nl} 2(2l+1)|\langle\varphi_{\mathbf{kl'}}|\delta\mathbf{V}|\varphi_{\mathbf{nl}}\rangle|^2, \tag{3}$$

where details of the calculation of the continuum wave functions ϕ_{kl} is given in Ref. [18]. Clearly, replacing δV in Eq. (3) by z yields the LDA cross section that entirely omits any correlations.

III. RESULTS AND DISCUSSION

A. He@C_{60}

Using the density-functional methodology, described above, calculations have been performed for the energies and wave functions of the ground states of the free He atom and the free C_{60} molecule, along with the energy levels and wave functions for He@C_{60}. In the combined system He@C_{60}, an interesting phenomenon occurs: hybridization. This effect is depicted in Fig. 1, where the wave functions of the free He $1s$ (localized in the atomic potential), the free C_{60} $2s$ (localized in the C_{60} shell potential), and the wave functions of these s states in the combined He@C_{60} system, which are termed $1s^+$ and $1s^-$ are shown. It is clear from Fig. 1 that these s-state wave functions in the He@C_{60} system have significant amplitude in both the atomic and shell regions of the combined potential, i.e., a hybridized mixture of atomic and shell states. This phenomenon was seen earlier [26] and can be explained qualitatively via perturbation theory. The mixing coefficient from that point of view is the matrix element of the perturbing potential between the unperturbed atomic and shell states divided by the (unperturbed) energy difference. This suggests that strong hybridization will occur whenever there is a large matrix element or near degeneracy (or both) between atomic and shell states of the same angular momentum; in this particular instance, the unperturbed states are not nearly

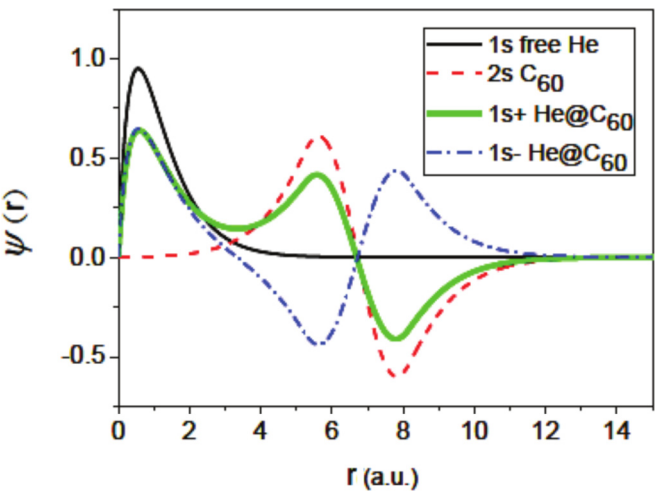

FIG. 1. (Color online) Wave functions of $1s$ of free He, $2s$ of C_{60}, and hybridized states of He@C_{60} are shown.

degenerate, but they do overlap significantly. In this case, the unperturbed energy of the He 1s state, 1.028 a.u., lies roughly halfway between $1s$ (1.392 a.u.) and $2s$ (0.645 a.u.) of free C_{60} (see Table I), so there is no near degeneracy. However, as seen in Fig. 1, there is some overlap between He $1s$ and C_{60} $2s$, which results in a large interaction matrix element and significant hybridization. On the other hand, there is essentially no hybridization between $1s$ of He and $1s$ of C_{60}, even though the energy difference between these states is about the same as $1s$ of He with $2s$ of C_{60} because there is almost no overlap between the two 1s wave functions. The fact that there is no hybridization between states of differing angular momentum results because the Hamiltonian of the system is spherically symmetric and thereby commutes with the orbital angular momentum operator; thus, the matrix element of the Hamiltonian between states of different orbital angular momentum vanishes.

It is of interest to note that the binding energies of the two hybridized states $1s^+$ and $1s^-$ are about 0.663 and 0.687 a.u., quite close to the energy of the unperturbed C_{60} $2s$ state (0.645 a.u.) but quite far from the $1s$ energy (1.028 a.u.) of free He. This is not accidental. In the combined system, the potential of the He atom perturbs the shell states, while the shell potential perturbs $1s$ of He. Since the shell potential is so much larger than the atomic potential, in a general sense, it is evident that, in the combined system, the atomic energy levels should be altered much more than the energies of the shell states. This is exactly what is found numerically for $He@C_{60}$. Furthermore, as a corollary, this implies that in cases where there is no hybridization, the atomic energies of the combined system will experience much greater changes from the unperturbed energies than what will be the case for the shell state energies.

Using these initial-state wave functions, the photoionization cross sections are obtained using the TDLDA methodology as described in the previous section. Since He has just a single $1s$ shell and this $1s$ is hybridized, as discussed above, it is no longer possible to ask how the confining shell modifies the He photoionization cross section; all one can do is to look at the cross sections of the various subshells of the combined $He@C_{60}$ system. In Fig. 2 the cross sections for the hybridized states $1s^+$ and $1s^-$ are shown along with the cross sections of the states that mix to form these hybridizations, the free He $1s$ and free C_{60} $2s$ states. The free He $1s$ cross section is seen to be featureless and monotonically decreasing from the threshold value of about 8 Mb. The free C_{60} $2s$ cross section is significantly larger, more than 30 Mb, in the threshold region (note the logarithmic scale), which is somewhat below the He $1s$ threshold, where it contributes to the well-known plasmon resonance in free C_{60} [22]. At higher energy, it falls off very rapidly, falling below the He $1s$ cross section around the He $1s$ threshold despite a second maximum in the 40-eV region contributing to the second (much smaller) C_{60} plasmon and dropping much faster than He $1s$ at still higher energies. In addition, the free C_{60} $2s$ cross section exhibits numerous minima as a result of strong oscillations with primary frequencies being related to the shell diameters from the interference of photoelectrons from inner and outer edges of C_{60} [32,34]. These minima are analogous to the Cooper minima of atoms but due to the nodes in continuum waves [35]. Thus, since the mixing of these state in the $1s^+$ and

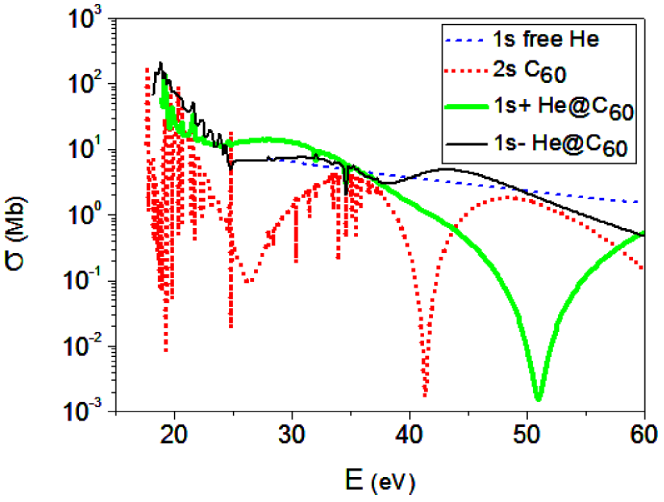

FIG. 2. (Color online) Cross sections of $1s$ of free He, $2s$ of C_{60}, and hybridized states of $He@C_{60}$ are shown.

$1s^-$ wave functions is roughly 50:50, it must be that the $1s^+$ and $1s^-$ cross sections emulate C_{60} $2s$ in the near-threshold region, where the C_{60} $2s$ cross section is by far the larger, and will be much closer to the He $1s$ cross section at higher energies for a similar reason; this is exactly what is shown in Fig. 2. Both near-threshold $1s^+$ and $1s^-$ cross sections are quite large, compared to He $1s$, reflecting the influence of C_{60} $2s$, and at the larger energies, they are close to He $1s$. In the intermediate-energy region, where the two unperturbed cross sections are comparable, the $1s^+$ and $1s^-$ cross sections are complicated owing to the existence of interferences in the coherent addition of the matrix elements; the deep Cooper minimum in the $1s^+$ cross section at about 50 eV, which is not where the unperturbed C_{60} $2s$ cross section shows a Cooper minimum, exemplifies this behavior. This is the consequence of oscillations in hybrid ionization that shell radii, rather than diameters, are related to the dominant frequencies in this energy range [36]. Briefly, the cause of this behavior, described in detail in Ref. [36], is the following: The overlaps in the matrix elements of hybrid $1s^+$ and $1s^-$ orbitals produce, besides regular atomic-type contributions from the central region, also significant contributions from the inner and outer radii of the C_{60} shell where strong ionizing forces from the large derivatives of the potential exist. These local emissions interfere with the atomic-type emission to produce leading oscillations in the momentum space with the radii determining the frequency. As a result, frequencies are decreased to half of those in free C_{60} $2s$, double the wavelengths, leading to a blueshift of the minimum, as can be seen.

However, this cannot be the entire story. Looking carefully at Fig. 2, it is noted that both the $1s^+$ and $1s^-$ cross sections maximize at about 100 Mb in the threshold region, far larger than the free C_{60} $2s$ cross section. It is thus evident that the $1s^+$ and $1s^-$ cross sections are not simply fractions of the free C_{60} $2s$ cross section determined by the squares of the relative amplitudes of the discrete C_{60} $2s$ and hybridized wave functions in the shell region, depicted in Fig. 1. This implies that the change in the total potential engendered by the He atom inside the C_{60} cage changes not only the initial discrete

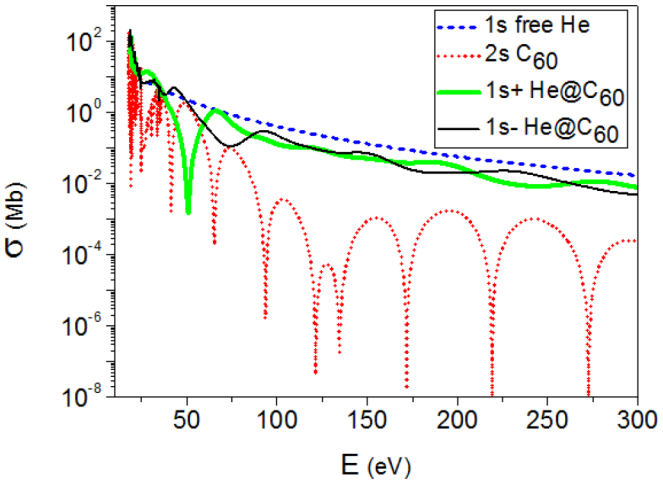

FIG. 3. (Color online) Cross sections of $1s$ of free He, $2s$ of C_{60}, and hybridized states of $He@C_{60}$ at higher energies are shown.

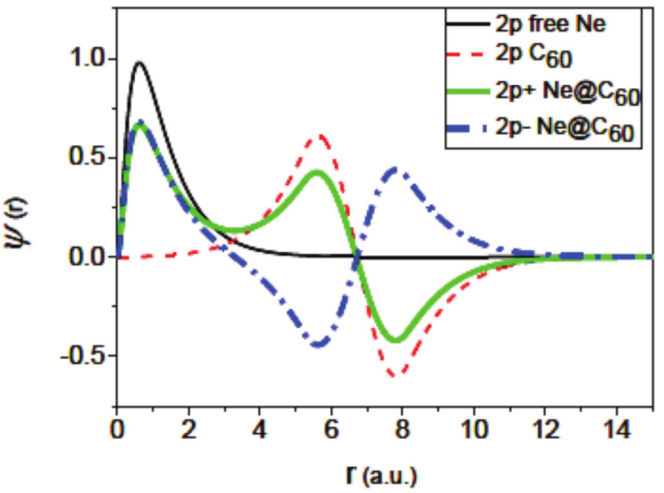

FIG. 4. (Color online) Wave functions of $2p$ of free Ne, $2p$ of C_{60}, and hybridized states of $Ne@C_{60}$ are shown.

wave functions, e.g., hybridization, but also the final-state wave functions and the interchannel coupling among them. It is known that interchannel coupling has a large effect upon the atomic photoionization cross sections of nonhybridized states of trapped atoms in the plasmon region [22], so it is no surprise that significant interchannel coupling exists for hybridized states as well. This is why the $1s^+$ and $1s^-$ cross sections are both significantly larger than the free C_{60} $2s$ cross section in the threshold region, which is also the energy region of the lower-energy C_{60} plasmon; the interchannel coupling caused mixing of the $1s^+$ and $1s^-$ channels with the matrix elements of the (very large) C_{60} photoionization channels contributing to the plasmon.

At the higher energies, shown in Fig. 3, it is evident that both the $1s^+$ and $1s^-$ cross sections are dominated by the contribution of He $1s$. The $1s^+$ and $1s^-$ cross sections are seen to be about equal in magnitude, except for the oscillations exhibited by both, oscillations not seen in the unperturbed He $1s$ cross section. These oscillations are known as confinement resonances [29,37], or confinement oscillations [30], and are the result of interferences of the continuum photoelectron wave emerging directly and after reflection from the inner or outer edges of the confining potential. In fact, the mechanism is richer than that. For hybrid orbitals photoelectrons emanated collaterally from the C_{60} region coherently combine with direct and reflective contributions [30]. A complete diagnosis of these multichannel interference oscillations, revealing frequencies related to the molecular geometry, was performed earlier [36]. These oscillations are ubiquitous and always occur for atoms confined in a potential [26,29]. However, the details of these confinement oscillations differ from atom to atom and even from subshell to subshell within a given atom. Looking at Fig. 3, it can be seen that the $1s^+$ and $1s^-$ cross sections exhibit these oscillations of the same amplitude and period, which simply reflects the geometry of the confining potential.

However, the details of the phases of these oscillations, exactly where the maxima and minima are, also involve the details of the atomic wave functions. This notion shall be reinforced as the photoionization cross sections of the other noble gases are presented below. Note also that interchannel coupling is not important for the atomic cross sections in the higher-energy region where the cross sections of the C_{60} photoionization channels are not much larger than the free atomic cross sections; here they are smaller so that any mixing does not cause any appreciable change in the atomic cross sections.

B. $Ne@C_{60}$

Looking at $Ne@C_{60}$, the situation differs somewhat in that the entrapped atom, Ne in this case, is itself a multishell system. The $1s$ and $2s$ discrete wave functions, whose binding energies are calculated to be 33.17 and 1.71 a.u., respectively, do not exhibit any near degeneracy with the energy levels of C_{60} (Table I) and do not overlap appreciably with the C_{60} $1s$ or $2s$ wave functions; as a result, they are not hybridized. The Ne $2p$ state, on the other hand, with an energy of 0.89 a.u., does overlap with the C_{60} $2p$ state, which is bound by 0.62 a.u., and is hybridized, much like the He $1s$ case. The situation is shown in Fig. 4, where it is seen that the hybridized wave functions of the combined $Ne@C_{60}$ system, labeled $2p^+$ and $2p^-$, are roughly a 50:50 admixture of the Ne $2p$ and C_{60} $2p$ states.

The binding energies of the two hybridized p states of the $Ne@C_{60}$ system are found to be 0.64 and 0.66 a.u., quite close to the unperturbed $2p$ state of free C_{60}. This is substantially the same as the He case, discussed above, and occurs for the same reason: The Ne potential perturbs the C_{60} by only a small amount percentagewise, but the C_{60} potential exerts a significant perturbation on the Ne atom, thereby resulting in the hybridized levels being much closer to unperturbed C_{60} than unperturbed Ne.

The cross sections for the free Ne and C_{60} $2p$ states, the states that mix to form the hybrids, are shown in Fig. 5, along with the hybridized state cross sections. The free Ne $2p$ cross section is seen to be relatively flat and featureless, except for the autoionizing resonances leading up to the $2s$ ionization threshold; these are $2s \rightarrow kp$ resonances. The nonresonant cross section can be seen to be a bit below 10 Mb over the entire range shown. The free C_{60} $2p$ state, on the other hand, shows a cross section that maximizes at close to 100 Mb in the

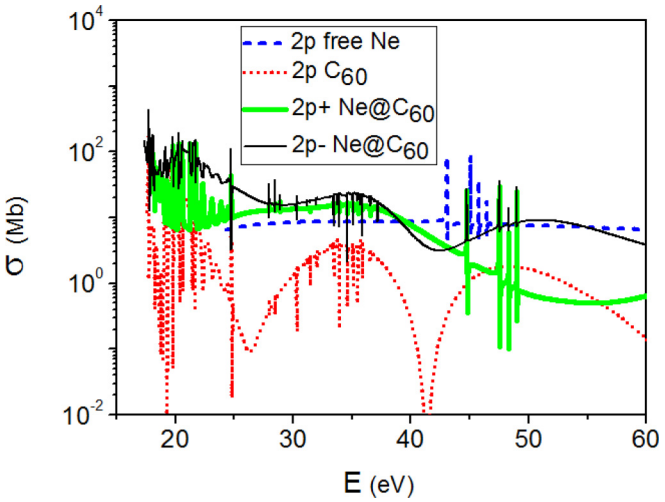

FIG. 5. (Color online) Cross sections of $2p$ of free Ne, $2p$ of C_{60}, and hybridized states of Ne@C_{60} are shown.

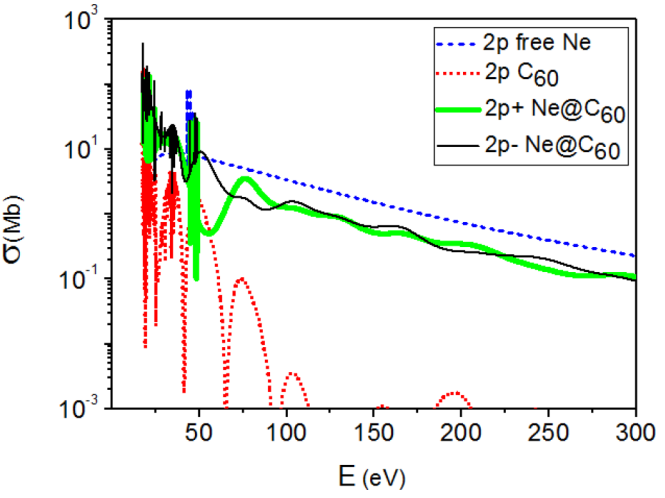

FIG. 6. (Color online) Cross sections of $2p$ of free Ne, $2p$ of C_{60}, and hybridized states of Ne@C_{60} at higher energies are shown.

20-eV (plasmon) region and shows another maximum in the 35-eV region, the region of the second C_{60} plasmon, which is somewhat obscured by a Cooper minimum just at 40 eV. The $2s \rightarrow kp$ resonances that are also seen in both the $2p^+$ and $2p^-$ cross sections occur at higher photon energy than is the case in free Ne. This occurs because the Ne $2s$ threshold energy in Ne@C_{60} increases by about 2.5 eV, as compared to free Ne; thus, the resonances are about 2.5 eV higher. Note that these resonances occur at exactly the same energies in the $2p^+$ and $2p^-$ cross sections, as they must; the resonance energies are a property of the resonances themselves, not the channels that they decay to. However, it is clear that the manifestation of these resonances in rather different in the $2p^+$ and $2p^-$ cross sections, as shown in Fig. 5.

In any case, in the threshold (plasmon) region, it can be seen from Fig. 5 that both the $2p^+$ and $2p^-$ cross sections are larger than the free C_{60} $2p$ cross section, similar to what was found for the He@C_{60} case. As in the He case, the reason for this is the interchannel coupling of these channels with the photoionization channels of C_{60} that contribute to the plasmons.

At the higher energies, the cross section is dominated by the atomic $2p$-like behavior since the C_{60} shell cross sections are much smaller here, as can be seen in Fig. 6. In addition, the confinement oscillations in both $2p^+$ and $2p^-$ cross sections are quite evident. These behaviors are quite the same as was seen in the He@C_{60} case and for the same reasons. The fact that the C_{60} shell cross sections for the $2p$ (and other) channels are so small in the higher-photon-energy region is a result of the delocalization of the valence orbitals. With increasing energy, the matrix element is generated closer and closer to the nucleus and delocalized orbitals by their very nature have small amplitude near the nucleus. Actually, the model potential used herein overemphasizes this effect somewhat by smearing out the effect(s) of the 60 carbon nuclei of the C_{60}. However, even using a more realistic model, these delocalized orbitals would not have much amplitude in the vicinity of the carbon nuclei, so the argument remains valid; at the higher energies the cross sections of the delocalized C_{60} states will be much smaller than the cross sections of the atomic orbitals, hybridized or not.

The $2s$ wave function of Ne is not hybridized in Ne@C_{60}, as discussed above. Furthermore, its ionization threshold is well above the plasmon region, so the C_{60} cross section is small, which means that one would not expect much in the way of interchannel coupling. In other words, the $2s$ photoionization cross section of confined Ne should be pretty much like the cross section for free Ne, except for the confinement oscillations brought about by the geometry of the confinement. This is exactly what happens, as shown in Fig. 7. These results are quite similar to what is predicted using a simple static model of the C_{60} potential on the trapped atom where interchannel coupling with C_{60} shell photoionization channels is omitted [14].

The confinement resonances are shown to decrease in amplitude with increasing energy, just as the simple model predicts [29,37,38]. Quantitatively, the amplitude was shown to have a $1/k^2$ behavior with k being the photoelectron

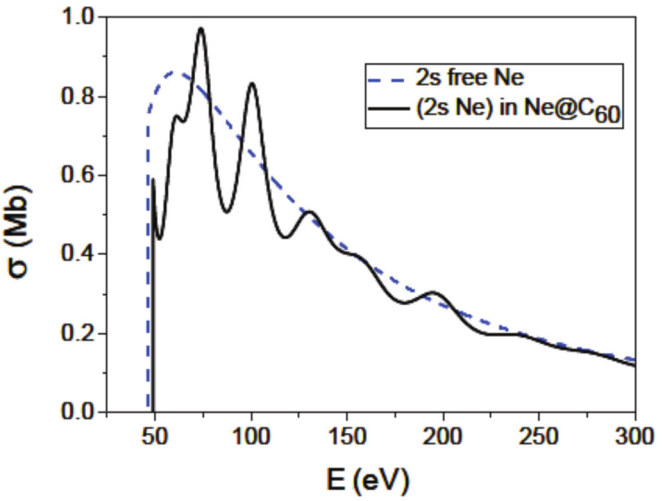

FIG. 7. (Color online) Cross sections of $2s$ of free Ne and $2s$ of Ne inside Ne@C_{60} are shown.

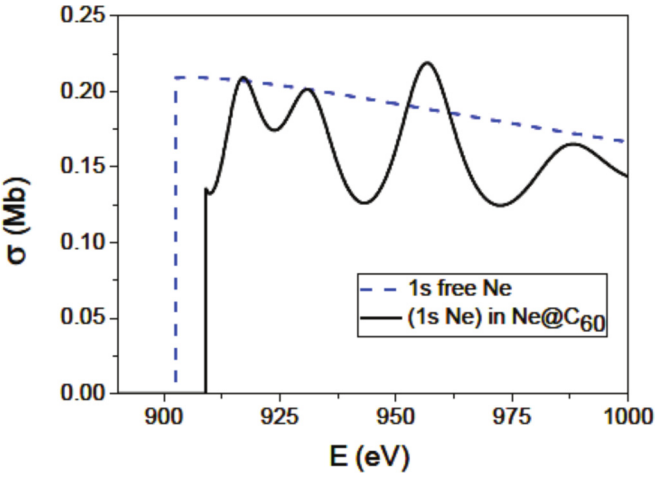

FIG. 8. (Color online) Cross sections of 1s of free Ne and 1s of Ne inside Ne@C_{60} are shown.

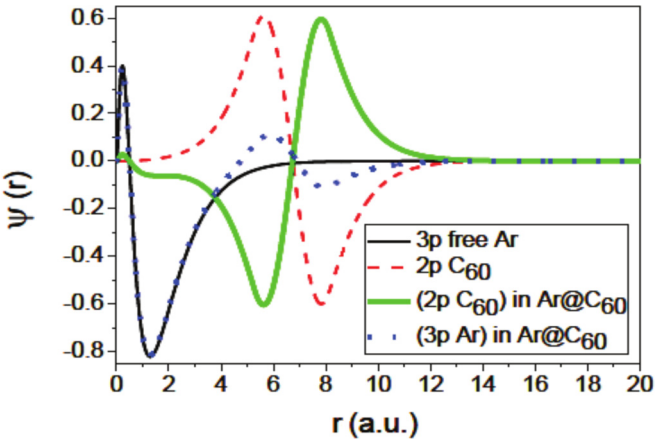

FIG. 9. (Color online) Wave functions of 3p of free Ar and 2p of C_{60} and atomic and shell states inside Ar@C_{60} are shown.

momentum [30]. This agreement with the simple model is further suggested by the 1s cross section of the trapped Ne atom, shown in Fig. 8. Here again, an atomiclike cross section is shown, modulated by confinement resonances.

It must be pointed out, however, that, since the 1s photoionization of the carbon atoms of the shell is omitted from the present calculation, any interchannel coupling of the Ne 1s cross section with the C 1s from the shell is of course omitted. However, interchannel coupling is only important when a channel with a small cross section is degenerate with a large one [39]. In this case, since the Ne 1s threshold is well above the C 1s threshold, the total cross section for 1s of all 60 carbon atoms of the shell, which can be estimated from the cross section for free carbon [40,41], is only slightly larger than the Ne 1s cross section. Thus, the omission is not likely to have a significant effect on the 1s photoionization of trapped Ne. In any case, scrutiny of the 1s and 2s photoionization of encaged Ne gives a good indication of where the simple model might be useful.

C. Ar@C_{60}

A previous calculation of 3p photoionization of Ar@C_{60} has been reported [23] using the same methodology as used herein, but completeness dictates that some of that presentation should be repeated. The situation for caged argon Ar@C_{60} is somewhat different from the previous cases in that no significant hybridization results in this case [23]. Of the Ar wave functions, only the 3p orbital shows any hybridization at all, as shown in Fig. 9.

Due to the entrapment, the C_{60} 2p orbital acquires a small image of the atomic 3p wave at small distances and the Ar 3p wave function exhibits a bit of the C_{60} 2p wave function at an intermediate distance from the center of the molecule. In other words, although they are slightly perturbed, the Ar 3p and C_{60} 2p wave functions retain their essential characters in the Ar@C_{60} molecule.

The 3p photoionization cross sections for free and confined Ar are shown in Fig. 10, where a remarkable difference between the two is noted: The confined 3p cross section is almost two orders of magnitude larger than its counterpart in free Ar. With increasing energy, this difference gets smaller, but remains until about 40 eV, or just above the higher-energy plasmon in C_{60}. To emphasize how large this difference really is, the integrated oscillator strength for 3p of free Ar from threshold to 40 eV is found to be about 4.85, or most of the six electrons in the 3p subshell. By way of comparison, the integrated oscillator for 3p of the confined atom is 60.2. This is greater than the total number of electrons in the Ar atom, not merely the six of the 3p subshell. Thus, since there is no appreciable hybridization of the 3p discrete wave function, this phenomenon must be due to correlation in the final (continuum) state of the photoionization process, interchannel coupling with the C_{60} photoionization channels. Furthermore, since the shell contains 240 nonlocalized electrons, it is evident that an appreciable fraction of the strength is transferred to the Ar 3p channel via interchannel coupling. Mathematically, this can be represented using the Fano continuum configuration-interaction formalism [42]. Defining the unperturbed (free) Ar 3p dipole matrix element as $D_{3p}(E)$ and the perturbed matrix

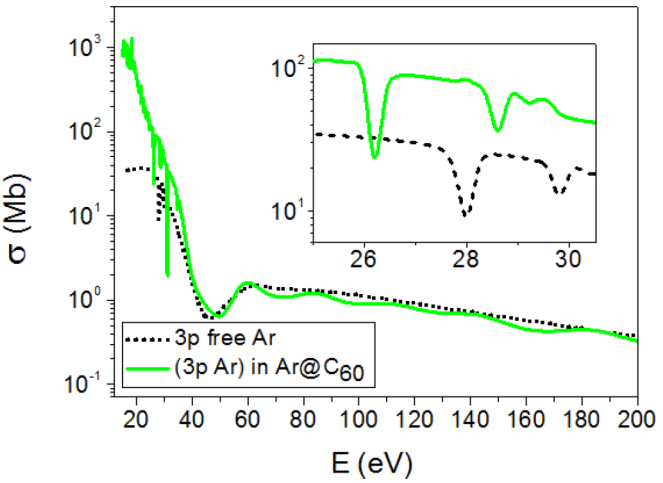

FIG. 10. (Color online) Cross sections of 3p of free Ar and 3p Ar inside Ar@C_{60} are shown; the inset shows the detail of the first two $3s \rightarrow kp$ resonances.

element (perturbed by interchannel coupling) as $M_{3p}(E)$, the perturbed matrix element, at energy E, is given by [25]

$$M_{3p}(E) = D_{3p}(E) + \sum_{nl} \int dE' \frac{\langle \psi_{nl}(E')|(1/r_{3p,nl})|\psi_{nl}(E)\rangle}{E - E'} D_{nl}(E'), \tag{4}$$

where ψ_{3p} and ψ_{nl} are the unperturbed final continuum state wave functions for $3p$ photoionization of free Ar and nl photoionization of the C_{60} shell, $r_{3p,nl} = |\mathbf{r_{3p}} - \mathbf{r_{nl}}|$, and the sum is over all of the delocalized electrons of the C_{60} shell. In the threshold region, where the perturbed $3p$ cross section is so much larger than the unperturbed, the second term in Eq. (4), the interchannel coupling term, dominates owing to the strength of the matrix elements of the delocalized electrons D_{nl}, which collectively form the huge plasmon in this energy region. With increasing energy, the interchannel coupling contributions become smaller, as the D_{nl} decrease with energy and the energy denominator in Eq. (4) reduces the contributions from the low-energy plasmon region. By 40 eV, interchannel coupling is relatively unimportant.

Looking at the higher energies, shown in Fig. 10, the Cooper minimum [43] in the free $3p$ cross section is seen in the 40-eV region and this Cooper minimum is reproduced in the confined cross section just a few eV higher. Above the Cooper minimum region, the free and confined cross sections are quite similar, except for the confinement oscillations exhibited by the confined cross section. Since the Cooper minimum is so sensitive to any kind of interaction with the system or correlation effect [44], it is clear that the effect of the cage on the $3p$ cross section is quite small, from the energy of the Cooper minimum region and above; this indicates further that the simple static model should be adequate in this energy region.

Also evident in both the free and confined $3p$ cross sections, shown in detail in the inset, are the $3s \rightarrow kp$ resonances that appear as window resonances in both cases; these window resonances are known experimentally for the free Ar atom. However, it can also be seen that these resonances show up at lower photon energy in the confined case, reflecting the fact that the Ar $3s$ subshell is less bound in the confined case. It can also be seen that the confinement affects not only the position of these resonances, but their detailed shape and width as well, thereby indicating that the interaction with the confining shell affects not only the binding energies of the confined atom, but also the dynamics of transition processes as well.

The calculated photoionization cross section of the $3s$ subshell of free and confined Ar is presented in Fig. 11. For free Ar, the dominant feature in the cross section is a very deep Cooper minimum at about 40 eV.

It is known that this feature results from interchannel coupling within the free Ar atom [45]; the result also agrees reasonably well with experiment [46]. In the confined case, at the lower energies, near the $3s$ ionization threshold, the $3s$ cross section is enhanced considerably, by a factor of 5 or so, owing to interchannel coupling with the photoionization channels of the C_{60} shell. The is similar to what happens for $3p$, as discussed above, but the effect is much smaller since the

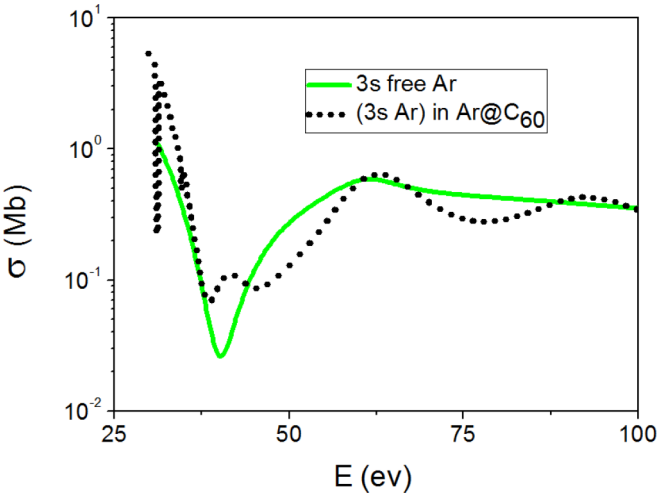

FIG. 11. (Color online) Cross sections of $3s$ of free Ar and $3p$ Ar inside Ar@C_{60} are shown.

shell cross sections drop very rapidly above the first plasmon at about 20 eV.

Furthermore, the confinement oscillations can be clearly seen in the confined Ar $3s$ cross section above about 30 eV and, as expected, their amplitudes diminish with increasing energy. The details of the Cooper minimum are altered somewhat from the free case owing to a combination of the dynamical effects of interchannel coupling, along with the confinement oscillations.

D. Kr@C_{60}

The situation for Kr is rather similar to that for Ar. The $4p$ wave function of Kr and the $2p$ orbital of C_{60} are *very slightly* hybridized, as shown in Fig. 12; this is almost exactly like the situation for Ar.

In addition, also like Ar, the outer ns, the $4s$ in this case, is not hybridized at all. The calculated free and confined Kr $4p$ cross sections are shown in Fig. 13 in the lower-energy region where it can be seen that interchannel coupling in

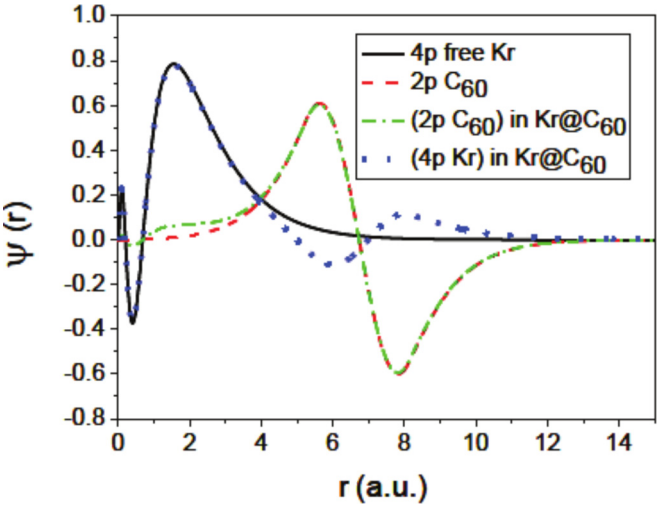

FIG. 12. (Color online) Wave functions of $4p$ of free Kr, $2p$ of C_{60}, and atomic and shell states inside Kr@C_{60} are shown.

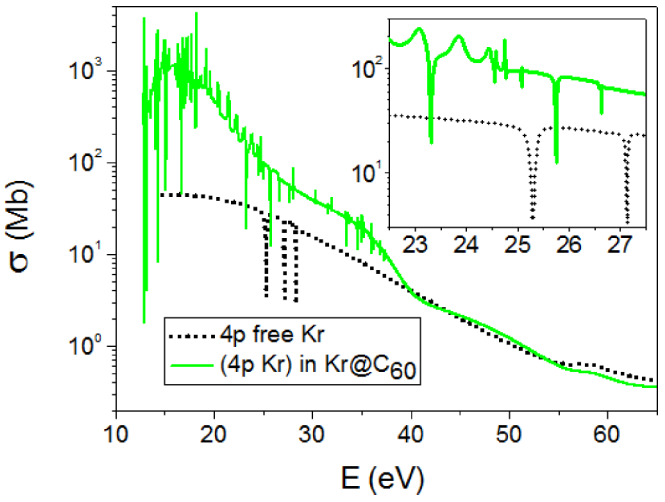

FIG. 13. (Color online) Cross sections of $4p$ of free Kr and $4p$ Kr inside Kr@C_{60} are shown; the inset shows the detail of the first two $4s \rightarrow kp$ resonances.

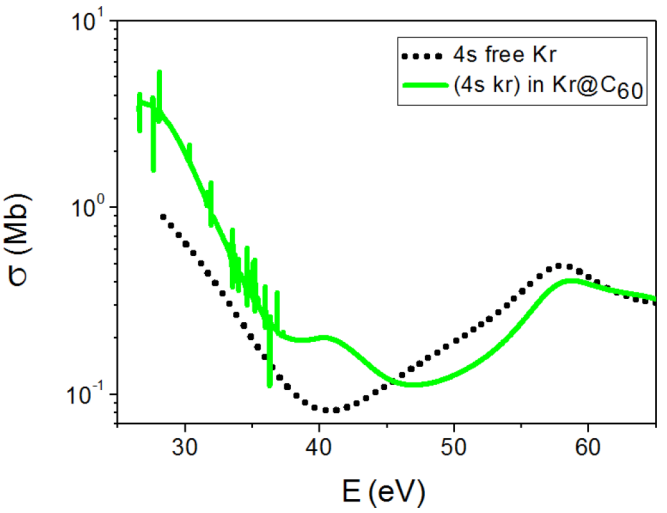

FIG. 15. (Color online) Cross sections of $4s$ of free Kr and $4s$ Kr inside Kr@C_{60} are shown.

the confined case increases the cross section by almost two orders of magnitude in the threshold region; as in the Ar case, this occurs because the photoionization cross section (matrix element) for the C_{60} channels in the plasmon region, just below 20 eV, is so much larger than the atomic cross section. At the end of the plasmon region, about 40 eV, this inequality no longer exists and the free and confined cross section more or less come together, except for the confinement resonances for the trapped atom

The window resonances $4s \rightarrow kp$ just below the opening of the 4s channel (shown in detail in the inset of Fig. 13) can also be seen in the free cross section and at lower energies in the confined cross section reflecting the decrease in binding energy engendered by the confinement. Also, like in the Ar case, the confinement is shown to result in more than just a global shift, indicating dynamics at work.

At higher energies, shown in Fig. 14, a broad Cooper minimum can be seen in both free and confined cross sections

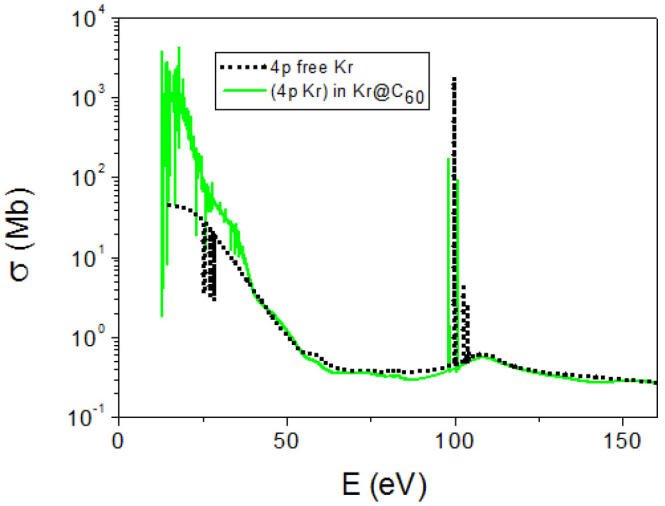

FIG. 14. (Color online) Cross sections of $4p$ of free Kr and $4p$ Kr inside Kr@C_{60} at higher energies are shown.

along with strong resonances in the 100-eV region, just below the $3d$ threshold, in both cases. Then a second maximum in the cross sections can be seen as they recover from the Cooper minima. Thus, above about 40 eV, except for confinement resonances and shifts in energy due to the cage potential, the free and confined results are almost the same; this means that in the energy region from 40 eV, the simple static model should be a reasonable approximation, in this case.

The $4s$ cross sections are shown in Fig. 15 and they behave rather like the $3s$ cross sections of Ar. In the threshold region, about 25 eV, the confined cross section is enhanced via interchannel coupling by a factor of about 4. Further, this enhancement decreases with increasing energy as we move to the edge of the plasmon region at about 35 eV. Both free and confined cross sections are seen to exhibit Cooper minima; again the primary cause of these Cooper minima is interchannel coupling among the atomic photoionization channels, but the Cooper minimum in the confined case is perturbed by the confinement potential along with the attendant confinement oscillations.

A similar situation is exhibited for Kr $3d$ photoionization as shown in Fig. 16. Owing to the $d \rightarrow f$ shape resonance [47], the cross section for free Kr is rising from threshold. Further, since the threshold energy, over 100 eV, is so far above the plasmon region of C_{60}, interchannel coupling with the photoionization channels of the shell is of essentially no consequence.

Thus, the cross section for the confined case is essentially just the free cross section modulated by confinement oscillation, clearly shown in Fig. 16. Evidently the high initial-state angular momentum (this is the first d state encountered) engenders no new behavior related to confinement.

E. Xe@C_{60}

Several aspects of the photoionization of confined Xe have been reported previously [18], but some repetition is necessary herein to fully depict the evolution along the sequence of noble-

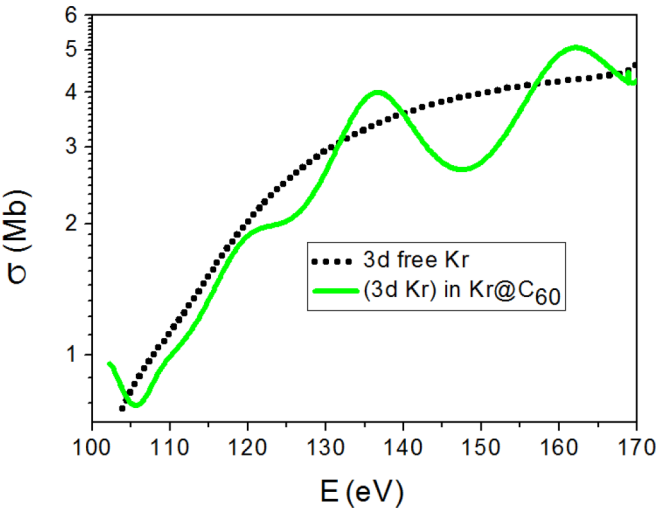

FIG. 16. (Color online) Cross sections of 3*d* of free Kr and 3*d* Kr inside Kr@C_{60} are shown.

gas atoms. Similar to Ar and Kr, the outer *p* subshell, 5*p* in this case, is only slightly hybridized, as shown in Fig. 17.

Unlike the previous two cases, however, the outermost *s* subshell 5*s* displays significant hybridization, as shown in Fig. 18. The hybridization is with the 2*s* subshell of C_{60}, just as was the case with confined He, discussed above. The mixing is seen to be roughly 50:50. The theoretical binding energy of Xe 5*s* is calculated to be 0.839 a.u., which is reasonably close to the 2*s* binding energy in free C_{60} of 0.645 a.u. (Table I). The binding energies of the hybridized orbitals $5s^+$ and $5s^-$ are 0.733 and 0.665 a.u., respectively; the latter is close to the free C_{60} 2*s* binding energy, but the former is roughly halfway between the two. This is different from the previous cases of hybridization where the hybridized orbitals were found to have binding energies quite close to the free C_{60} component. This is because in this case, the atomic potential, which supports 54 electrons, is not so very small compared to the shell potential.

The calculated free and confined 5*p* cross sections are displayed in Fig. 19(a) and a picture similar to the corresponding

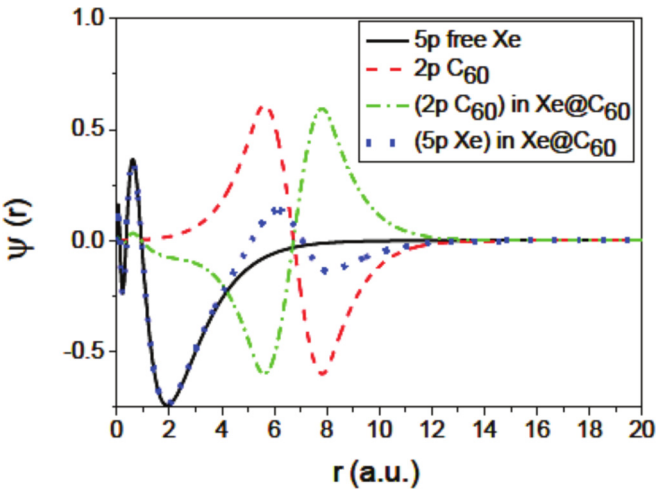

FIG. 17. (Color online) Wave functions of 5*p* of free Xe, 2*p* of C_{60}, and atomic and shell states inside Xe@C_{60} are shown.

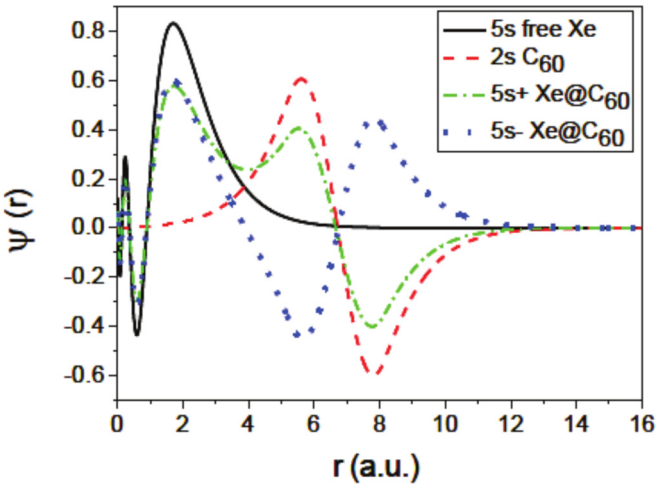

FIG. 18. (Color online) Wave functions of 5*s* of free Xe, 2*s* of C_{60}, and hybridized states of Xe@C_{60} are shown.

outer *np* subshell in Ar and Kr can be seen. As in those cases, the confined cross section is almost two orders of magnitude larger than the atomic cross section owing to interchannel coupling with the huge C_{60} plasmon excitations; the confined 5*p* cross section displays the effects of coupling with both of the plasmons, the larger one at the lower energies and the smaller one at the higher energies. Above the energy region of the plasmons, the confined cross section is similar to the free 5*p* cross section, except for the confinement oscillations. The $5s \rightarrow kp$ resonances, shown as window resonances in the atomic cross section below the opening of the 5*s* channel in Fig. 19(b), are difficult to pick out in the confined cross section since they occur in a region of many resonances involving transitions to hole states in the C_{60} shell. There must actually be two sets of resonances, a $5s^+ \rightarrow kp$ series and a $5s^- \rightarrow kp$ series, offset by different energy shifts owing to the different binding energies of the two hybridized levels, but they do not appear to show up as window resonances in the confined case and seem to be mixed with the C_{60} resonances in this hybridized case. This differs from the Ar and Kr results, evidently because of the hybridization of the 5*s* orbital in confined Xe.

The cross sections for the hybridized $5s^+$ and $5s^-$ states of the combined Xe@C_{60} system are shown in Fig. 20, along with the cross sections of 5*s* of free Xe and 2*s* of free C_{60}. It is striking that both the $5s^+$ and $5s^-$ cross sections are approximately an order of magnitude larger than the cross sections of the free Xe and free C_{60} constituents of these hybridized states. Clearly then, interchannel coupling in the final continuum states also plays a crucial role in the determination of these cross sections.

In fact, evidence of the influence of the C_{60} plasmons can be seen in the maxima in the 20-eV region and the maxima a bit below 40 eV. In any case, this is another instance of both the initial state and the final state of a photoionizing transition losing their identity in the combined system.

The 4*d* cross sections for the free and confined systems are presented in Fig. 21. Since the 4*d* threshold energies are well above the plasmon region, no important interchannel coupling effects of the 4*d* cross section with the shell channels are

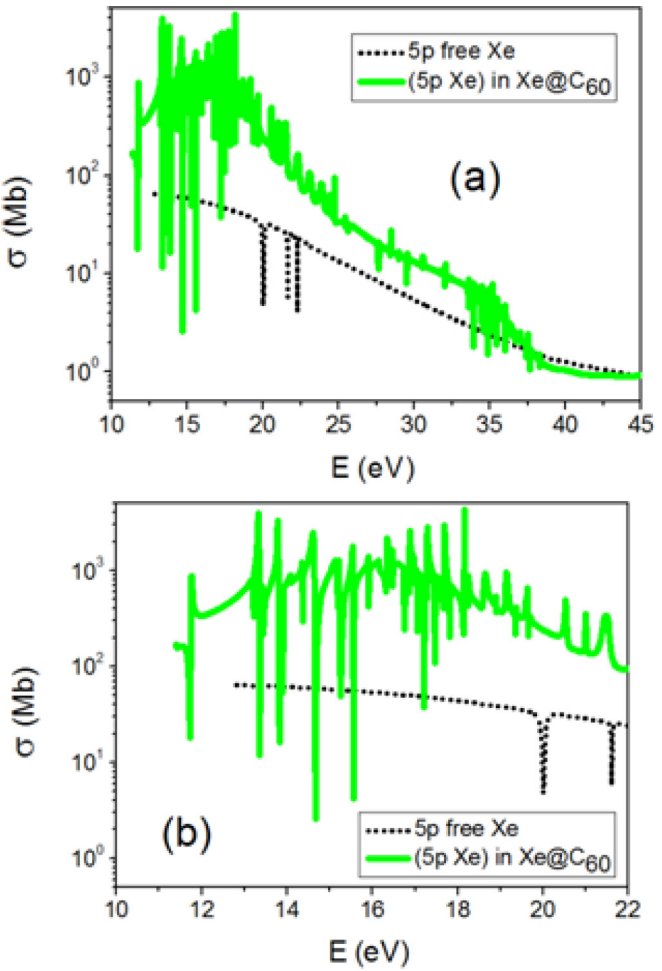

FIG. 19. (Color online) Cross sections of $5p$ of free Xe and $5p$ Xe inside Xe@C_{60} are shown between (a) 10 and 45 eV and (b) 10 and 22 eV where the first two $5s \rightarrow kp$ resonances in free Xe are shown.

expected and none are seen. However, significant confinement oscillations are evident. Note that confinement oscillations in the $4d$ subshell of Xe@C_{60} have been observed experimentally [10–12] using the Advanced Light Source (ALS) synchrotron source and show prominent peaks at photon energies of about 90 and 110 eV, as compared to the present results, which show the peaks at roughly 100 and 120 eV. This discrepancy indicates that, although the present calculations are qualitatively correct, there are some quantitative deficiencies. A possible contribution to the difference could be due to the error in the $4d$ binding energy, which is too large for free Xe by about 7.5 eV, 75 eV vs 67.5 eV [41]. Assuming that the same difference persists for the confined atom, this accounts for a significant percentage of the difference after transforming to the photoelectron momentum scale, the true scale of the oscillations. The peaks will still remain off as a function of photoelectron energy, but by a reduced amount.

Another cause of discrepancy between our TDLDA results and measurements could be due to a possible phase offset between the theoretical single-photoionization cross section and experimental double-photoionization data. However, since the origin of the confinement oscillations is still fundamentally geometric, several inherent similarities between the TDLDA

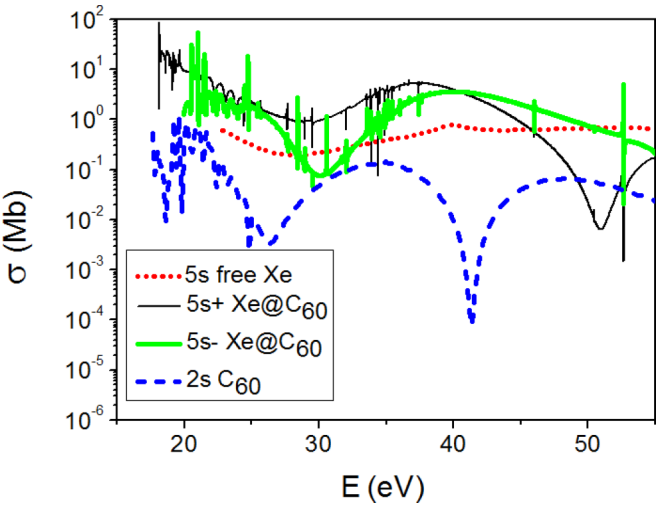

FIG. 20. (Color online) Cross sections of $5s$ of free Xe, $2s$ of C_{60}, and hybridized states are shown.

prediction and the ALS data have recently been obtained by transforming the signal to the Fourier reciprocal space [48], a method that can efficiently separate the frequency signals of correct oscillations from the "wrong" ones due to fluctuations from poor statistics in the experiment. Finally, of course, there could also be discrepancies due to the use of a jellium spherical well to approximate the field of the 60 C^{4+} ions of the C_{60} shell. In any case, the notion that confinement oscillations might be mythical, as suggested recently [49], is certainly not borne out. In addition to the smooth nonresonant cross section, Rydberg resonances are seen in the 150- and 190-eV regions of the cross sections.

These are the resonances leading up the $4p$ and $4s$ thresholds, respectively. The resonances are displaced slightly between the free and confined cross sections owing to the slight differences in threshold energies engendered by the confinement.

Finally, the free and confined 4p cross sections are shown in Fig. 22. The $4p$ cross sections are small and the confined cross section is similar to the free, except for

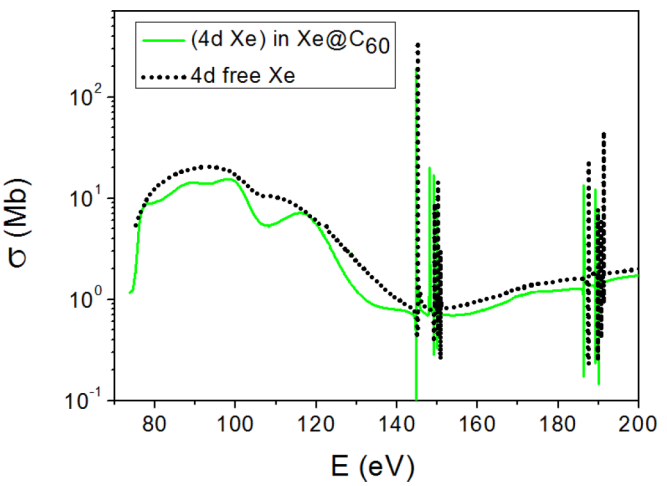

FIG. 21. (Color online) Cross sections of $4d$ free Xe and $4d$ Xe inside Xe@C_{60} are shown.

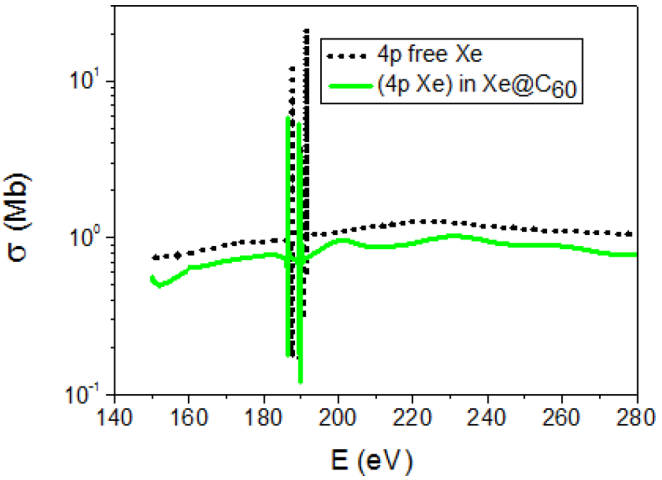

FIG. 22. (Color online) Cross sections of 4p free Xe and 4p Xe inside Xe@C_{60} are shown.

the confinement oscillations. However, the confined cross section is everywhere about 10% below the free cross section, indicating that the confinement induces more than simply a modulation about the free cross section. Most likely, the small overall decrease in cross section arises from small differences in interchannel coupling among the atomic photoionization channels. The Rydberg resonances below the opening of the 4*s* channel can be seen in this case, just as in the 4*d* cross section.

IV. CONCLUSION

Calculations of the photoionization of the outer and intermediate subshells of the noble-gas atoms He through Xe, confined at the center of the fullerene molecule C_{60}, have been performed using a time-dependent local-density approximation methodology. The systematics of the photoionization of outer and near-outer subshells of the confined noble gases is now understood and should provide an impetus for further experimental investigations. Specifically, the results show confinement oscillations predicted generally in the confined cross sections of all subshells of all atoms. In the lower-energy region, the region of the plasmons in the free C_{60} cross section, it was found that interchannel coupling dramatically increased the cross sections of the entrapped atoms in all cases. Mixing between bound-state wave functions of the C_{60} shell and the enclosed atom, hybridization, was found in a number of cases, but there appear to be no obvious systematics to which subshells of atoms are hybridized and the phenomenon of hybridization plus interchannel coupling affecting a single transition was noted and explained. It was also noted that the binding energies of the hybridized states tended to be much closer to the energies of the C_{60} component of the hybrid and this was explained in terms of the relative sizes of the perturbation to each state. For the same reasons, the nonhybridized atomic energy levels are affected much more by the confinement than the shell energies. It is important to note that these effects should be generally in evidence for the photoionization of any atom confined at the center of C_{60}.

Inner shells (except Xe 4*d*) of confined atoms have hardly been studied previously. Here the photoionization of a number of inner shells have been scrutinized; we have learned how interchannel coupling becomes less important but interaction with the shell still alters and/or moves atomic features. Confinement resonances are found to be prominent for inner shells and many cross sections show not only the resonances but also an overall magnitude change, i.e., the situation is much more complicated than just confinement resonances. In addition, insight into the behavior of inner-shell excitations, Rydberg resonances, and how their energies and shapes are altered by the confinement has been garnered.

It was also shown that at energies away from the C_{60} plasmon resonances, i.e., above the photon energy of 40 eV or so, in cases where there is little or no hybridization, the simple static model should be adequate to describe the photoionization of confined atoms. From a practical point of view, this means inner subshells with binding energies greater than about 40 eV; not only do they miss the plasmon region, but their wave functions are so compact that there is essentially no overlap with the shell wave functions, so no hybridization occurs.

The only relevant experimental results involve studies of the 4*d* subshell Xe@C_{60} [11,12], which confirmed the existence of confinement resonances. A detailed comparison [11,12] with essentially the same calculation reported in this paper showed good qualitative agreement, but quantitative discrepancies; some of the reasons for these were discussed.

Where do we go from here? Among the improvements or enhancements that are required is a relaxation of spherical symmetry, which would allow the treatment of atoms trapped inside a fullerene but off center and atoms confined in nonspherical fullerenes. Certainly, a fully molecular treatment would alter the energy levels and wave functions of the various levels of free C_{60} and this would have some effect upon the photoionization of atoms confined in the C_{60}. The one major effect that this might have is on hybridization, which is very dependent upon the wave functions and the relative energies of the hybrid and shell states. In addition, the jellium potential overdelocalizes the valence electrons with the consequence of predicting C_{60} plasmon positions slightly redshifted from the experimental values as a result of the missing restoring force that would exist for a truncated icosahedron core [22]. Besides these, nowhere else are the C_{60} wave functions and energies of crucial importance.

In addition, the *K*-shell photoionization of the carbon atoms making up the C_{60} shell, which was omitted in the present calculation, needs to be included. Finally, at the higher photoelectron energies, where the photoelectron wavelength becomes comparable with the separation of the carbon atoms in the fullerene shell, the discrete nature of these contributions to the potential must be included as opposed to a smeared-out jellium model. Clearly much work needs to be done.

ACKNOWLEDGMENTS

This work was supported by the NSF and DOE, Office of Basic Energy Sciences. H.S.C. acknowledges collaborations with Mohammed E. Madjet from QEERI, Qatar Foundation at Doha, which helped establish the ongoing fullerene research program.

[1] L. Dunsch and S. Yang, Small **3**, 1298 (2007).

[2] V. K. Dolmatov, A. S. Baltenkov, J.-P. Connerade, and S. T. Manson, Radiat. Phys. Chem. **70**, 417 (2004).

[3] V. K. Dolmatov, in *Advances in Quantum Chemistry: Theory of Quantum Confined Systems*, edited by J. R. Sabin and E. Brandas (Academic, New York, 2009), pp. 13–68.

[4] J.-P. Connerade, in *The Fourth International Symposium on Atomic Cluster Collisions: Structure and Dynamics from the Nuclear to the Biological Scale*, edited by A. V. Solovyev and E. Surdutovich, AIP Conf. Proc. No. 1157 (AIP, New York, 2009), pp. 1–33.

[5] W. Harneit, C. Boehme, S. Schaefer, K. Huebener, K. Fostiropoulos, and K. Lips, Phys. Rev. Lett. **98**, 216601 (2007).

[6] J. B. Melanko, M. E. Pearce, and A. K. Salem, in *Nanotechnology in Drug Delivery*, edited by M. M. de Villiers, P. Aramwit, and G. S. Kwon (Springer, New York, 2009), p. 105.

[7] R. B. Ross, C. M. Cardona, D. M. Guldi, S. G. Sankaranarayanan, M. O. Reese, N. Kopidakis, J. Peet, B. Walker, G. C. Bazan, E. V. Keuren, B. C. Holloway, and M. Drees, Nat. Mater. **8**, 208 (2009).

[8] Y. Zhao, Y.-H. Kim, A. C. Dillon, M. J. Heben, and S. B. Zhang, Phys. Rev. Lett. **94**, 155504 (2005).

[9] S. W. J. Scully, E. D. Emmons, M. F. Gharaibeh, R. A. Phaneuf, A. L. D. Kilcoyne, A. S. Schlachter, S. Schippers, A. Müller, H. S. Chakraborty, M. E. Madjet, and J. M. Rost, Phys. Rev. Lett. **94**, 065503 (2005).

[10] A. Müller, S. Schippers, M. Habibi, D. Esteves, J. C. Wang, R. A. Phaneuf, A. L. D. Kilcoyne, A. Aguilar, and L. Dunsch, Phys. Rev. Lett. **101**, 133001 (2008).

[11] A. L. D. Kilcoyne, A. Aguilar, A. Müller, S. Schippers, C. Cisneros, G. Alna'Washi, N. B. Aryal, K. K. Baral, D. A. Esteves, C. M. Thomas, and R. A. Phaneuf, Phys. Rev. Lett. **105**, 213001 (2010).

[12] R. A. Phaneuf, A. L. D. Kilcoyne, N. B. Aryal, K. K. Baral, D. A. Esteves-Macaluso, C. M. Thomas, J. Hellhund, R. Lomsadze, T. W. Gorczyca, C. P. Ballance, S. T. Manson, M. F. Hasoglu, S. Schippers, and A. Müller, Phys. Rev. A **88**, 053402 (2013).

[13] S. Lo, A. V. Korol, and A. V. Solov'yov, Phys. Rev. A **79**, 063201 (2009).

[14] M. Ya. Amusia, A. S. Baltenkov, and L. V. Chernycheva, J. Phys. B **41**, 165201 (2008), and references therein.

[15] V. K. Dolmatov and S. T. Manson, J. Phys. B **41**, 165001 (2008), and references therein.

[16] K. Govil, A. J. Siji, and P. C. Deshmukh, J. Phys. B **42**, 065004 (2009), and references therein.

[17] M. Stener, G. Fronzoni, D. Toffoli, P. Colavita, S. Furlan, and P. Decleva, J. Phys. B **35**, 1421 (2002).

[18] M. E. Madjet, T. Renger, D. E. Hopper, M. A. McCune, H. S. Chakraborty, J.-M. Rost, and S. T. Manson, Phys. Rev. A **81**, 013202 (2010).

[19] Z. Chen and A. Z. Msezane, Phys. Rev. A **86**, 063405 (2012).

[20] T. W. Gorczyca, M. F. Hasoglu, and S. T. Manson, Phys. Rev. A **86**, 033204 (2012).

[21] J. Jose and R. R. Lucchese, J. Phys. B **46**, 215103 (2013).

[22] M. E. Madjet, H. S. Chakraborty, J. M. Rost, and S. T. Manson, J. Phys. B **41**, 105101 (2008).

[23] M. E. Madjet, H. S. Chakraborty, and S. T. Manson, Phys. Rev. Lett. **99**, 243003 (2007).

[24] H. S. Chakraborty, M. E. Madjet, J.-M. Rost, and S. T. Manson, Phys. Rev. A **78**, 013201 (2008).

[25] M. H. Javani, M. R. McCreary, A. B. Patel, M. E. Madjet, H. S. Chakraborty, and S. T. Manson, Eur. Phys. J. D **66**, 189 (2012).

[26] H. S. Chakraborty, M. E. Madjet, T. Renger, J.-M. Rost, and S. T. Manson, Phys. Rev. A **79**, 061201(R) (2009).

[27] J. N. Maser, M. H. Javani, R. De, M. E. Madjet, H. S. Chakraborty, and S. T. Manson, Phys. Rev. A **86**, 053201 (2012).

[28] M. J. Puska and R. M. Nieminen, Phys. Rev. A **47**, 1181 (1993); **49**, 629 (1994).

[29] J.-P. Connerade, V. K. Dolmatov, and S. T. Manson, J. Phys. B **33**, 2279 (2000).

[30] M. A. McCune, M. E. Madjet, and H. S. Chakraborty, Phys. Rev. A **80**, 011201(R) (2009).

[31] O. Gunnerson and B. Lundqvist, Phys. Rev. B **13**, 4274 (1976).

[32] A. Rüdel, R. Hentges, U. Becker, H. S. Chakraborty, M. E. Madjet, and J. M. Rost, Phys. Rev. Lett. **89**, 125503 (2002).

[33] M. E. Madjet, H. S. Chakraborty, and J. M. Rost, J. Phys. B **34**, L345 (2001).

[34] M. A. McCune, M. E. Madjet, and H. S. Chakraborty, J. Phys. B **41**, 201003 (2008).

[35] K. Jänkälä, M. Tchaplyguine, M.-H. Mikkelä, O. Björneholm, and M. Huttula, Phys. Rev. Lett. **107**, 183401 (2011).

[36] A. Potter, M. A. McCune, R. De, M. E. Madjet, and H. S. Chakraborty, Phys. Rev. A **82**, 033201 (2010).

[37] A. S. Baltenkov, Phys. Lett. A **254**, 203 (1999).

[38] Y. B. Xu, M. Q. Tan, and U. Becker, Phys. Rev. Lett. **76**, 3538 (1996).

[39] D. L. Hansen, O. Hemmers, H. Wang, D. W. Lindle, P. Focke, I. A. Sellin, C. Heske, H. S. Chakraborty, P. C. Deshmukh, and S. T. Manson, Phys. Rev. A **60**, R2641 (1999), and references therein.

[40] R. F. Reilman and S. T. Manson, Astrophys. J. Suppl. **40**, 815 (1979).

[41] E. B. Saloman, J. H. Hubbell, and J. H. Scofield, At. Data Nucl. Data Tables **38**, 1 (1988).

[42] U. Fano, Phys. Rev. **124**, 1866 (1961).

[43] J. W. Cooper, Phys. Rev. **128**, 681 (1962).

[44] A. F. Starace, in *Handbuch der Physik*, edited by W. Mehlhorn (Springer, Berlin, 1982), Vol. 31, pp. 1–121.

[45] M. Ya Amusia, *Atomic Photoeffect* (Plenum, New York, 1990), and references therein.

[46] V. Schmidt, Rep. Prog. Phys. **55**, 1483 (1992), and references therein.

[47] S. T. Manson and J. W. Cooper, Phys. Rev. **165**, 126 (1968).

[48] A. B. Patel and H. S. Chakraborty, J. Phys. B **44**, 191001 (2011).

[49] A. V. Korol and A. V. Solov'yev, J. Phys. B **43**, 201004 (2010).